ELSEVIER

Fracture behaviour of a TiAl alloy under various loading modes

R. Cao [a,b], Y.Z. Lin [b], D. Hu [c], J.H. Chen [a,b,*]

[a] *State Key Laboratory of Gansu Advanced Non-ferrous Metal Materials, Lanzhou University of Technology, Lanzhou 730050, China*
[b] *Key Laboratory of Non-ferrous Metal Alloys, The Ministry of Education, Lanzhou University of Technology, Lanzhou 730050, China*
[c] *Interdisciplinary Research Centre in Materials, The University of Birmingham, Edgbaston, Birmingham B15 2TT, UK*

Abstract

Tensile tests, compression tests, in situ tensile tests, bending tests, tensile fatigue tests and bending fatigue tests were carried out for a TiAl alloy. Based on the global experimental results and microscopic observations of the fracture surfaces and cracking behaviour on the side surfaces of tested specimens, the fracture mechanisms of fully lamellar (FL) TiAl alloys under various loading modes are summarized as following: (1) Cracks initiate at grain boundaries and/or interfaces between lamellae. (2) When a crack extends to a critical length, which matches the fracture loading stress the crack propagates catastrophically through entire specimen. (3) The crack with the critical length can be produced promptly by the applied load in the tensile and bending test or be produced step-by-step by a much lower load in the fatigue tensile test. (4) For fatigue bending tests, the fatigue crack initiates and extends directly from the notch root, then extends step-by-step with increasing the fatigue bending loads. The fatigue crack maybe extends through entire specimen at a lower fatigue load or triggers the cleavage through the whole specimen at a higher load. (5) In compressive tests, cracks initiate and propagate in directions parallel or inclined to the compressive load after producing appreciable plastic strains. The specimen can be fractured by the propagation of cracks in both directions.
© 2008 Published by Elsevier Ltd.

Keywords: TiAl alloys; Fracture mechanisms; In situ tensile test; Fatigue; Compression

1. Introduction

The fracture behaviour of TiAl alloy has been investigated intensively over the past 20 years. Kim and Dimiduk described that the room temperature (RT) fracture in duplex phase (DP) TiAl alloy was dominantly transgranular cleavage-like failure, often exhibiting river patterns. Fully lamellar (FL) specimens exhibited three characteristic fracture features at RT: translamellar fracture, interlamellar fracture and a mixture depending on the lamellar orientation with respect to the crack path or stress axis [1]. Inui et al. [2] investigated the tensile deformation of polysynthetically twinned (PST) crystals of TiAl and found that the tensile

---

Nomenclature

$No.$	number of specimens (B, Birmingham materials; T, tensile tests; C, compression tests; S, in situ tensile tests; 3PB, three point bending tests; TF, tensile fatigue tests; 3PB-F, three point bending fatigure tests)
S_e	true area of original cross-section in the specimen's ligament
W	width of specimen
B	thickness of specimen
a	length of the slit notch
E	elastic modulus
$\sigma_{0.2}$	yield stress
ε_f	fracture strain
σ_f	fracture stress
σ_{UTS}	ultimate tensile strength
ε_u	unload strain
σ_u	unload stress
w'	fracture work per unit areas (the energy absorbed by unit area of specimen)
N	number of microcracks produced in the loading process
L_{max}	length of maximum crack
P_i	load of crack initiation
σ_i	stress of crack initiation
P_f	fracture load
P_{max}	maximum load
K_{max}	maximal stress intension factor
σ_{max}	maximum stress
σ_a	stress amplitude
σ_m	average stress
f	frequency
N_f	the number of cycles up to specimen failure
N_u	the number of cycles up to specimen unloading
σ_{max-n}	maximum nominal stress

elongation to fracture, as well as the yield strength, are strongly dependent on the inclined angle between the lamellar interfaces and tensile axis. The largest tensile elongation of 20% and the lowest yield strength around 100 MPa (lowest yield shear stress around 50 MPa) were obtained for specimens with an inclined angle of 31° (the soft orientation) whilst at 0° and 90° (the hard orientations) the elongation was reduced almost next to zero and the stress increased to 300–500 MPa. Akiyama et al. [3] studied directionally solidified ingots composed of columnar grains with the lamellae aligned at various angles with the crack propagation direction. They found that the fracture toughness of specimens with the lamellae perpendicular to the precrack was much higher than that of specimens with the lamellae parallel to the precrack. Many studies about fatigue life have been carried out [4–8]. It was reported in [5] that single monotonic overloading to a stress of 780 MPa ($0.95\sigma_{0.2}$) did not affect the subsequent fatigue life tested at $\sigma_{max} = 550$ MPa ($0.67\sigma_{0.2}$), indicating that the damage induced by that single overloading, if any, be not sufficient enough to cause failure during fatigue loading at the stress level. Overloading to a higher stress level of 830 MPa ($\sigma_{0.2}$) was found to have caused initiation of sufficient interlamellar damage at colonies on the tensile face which led to short fatigue life in 3 of 16 samples tested. The fatigue life at $\sigma_{max} = 550$ MPa ($0.67\sigma_{0.2}$), was affected after the samples had experienced 1k overloading cycles to $\sigma_{max} = 650$ MPa ($0.79\sigma_{0.2}$) during which damage was caused. An overview of the current understanding of the community on these issues is presented in [6] in which different fatigue properties of TiAl alloys, namely high cycle fatigue (HCF), cyclic stress–strain (CSS) behaviour and

fatigue crack growth (FCG) resistance were reviewed. The influence of different parameters (microstructure, defects, temperature and environment) on these properties was examined as well. In [7], the effects of low-cycle fatigue, 2×10^5 alternate bending cycles ($R = 0.1$), at high stress intensity levels, i.e., the fatigue limit, on mechanical behaviour of three different microstructures was evaluated. The data reported and discussed in [7] showed that bending fatigue training enhanced the mechanical behaviour of this material, mainly through the occurrence of a plastic deformation during the bending tests. In [9], the authors revealed a widely referred K-resistance curve, a plot of K versus crack extension length, which showed the low initiation toughness and the increasing fracture resistance with increasing crack extension. The fracture resistance was distinctly increased when the crack encountered unfavorably oriented colony boundaries. In [10], the authors further investigated the colony boundary resistance in relation to crack propagation by using single-colony thick specimens. In that study, the results revealed a very low load for crack initiation and a remarkable enhancement at a twist angle larger than 40° (Fig. 9 in [10]). Three figures (Fig 10(a)–(c) in [10]) also showed that a higher applied load was required to propagate the main crack. The present authors [11] indicated that in thin specimens, cracks preferred to initiate and propagate at the interfaces between lamellae. The driving force for fracture development was the tensile stress. The interlamellar cracks could be produced at a normal stress as low as around 50 MPa, which was lower than the yield stress in the soft orientation [2,12]. The interlamellae crack bypassed the grains with unfavorable orientation along the grain boundaries or stretched themselves through the grains by translamellar cracking. In authors' previous papers [13,14], two modes of fracture depending on the damage pattern were found: (a) A number of large interlamellar cracks were produced and made a weakest section. The final fracture occurred by the connection of these interlamellar cracks. The fracture stress was determined by the remaining area between these interlamellar cracks. (b) When a larger crack extended to a critical length matching the loading stress the crack propagated catastrophically through entire specimen. The fracture stress was determined by the critical length of the crack. In [14], the present authors found that the large lamellar cracks showed a rate-dependent character. The higher the loading rate, the lower the density of preceding microcracks or the shorter the critical crack and the higher the fracture stress.

With the development of TiAl alloys, in order to optimize microstructures, there is a need for both metallurgists and material designers to get insights into the mechanisms governing the fracture toughness and the fatigue properties of TiAl alloys. Fracture processes are different in different TiAl alloys at various loading modes. In this paper, the fracture behaviour under various monotonic loading modes and fatigue loading modes for a high quality TiAl alloy provided by The University of Birmingham were investigated.

2. Experimental procedure

2.1. Materials and specimens

A TiAl alloy with nominal composition of Ti–44Al–4Nb–5Hf–0.2Si–1B was used. The TiAl alloy was prepared via cold-hearth plasma arc-melting and casting into an ingot of 150 mm in diameter and 50 kg in weight. The ingot was melted twice to improve the chemical homogeneity. Ingot breakdown was carried out via extrusion (at 1200 °C and a ratio of 8:1). After extrusion the alloy was subjected to heat treatment of 1300 °C/1 h/FC to obtain fully lamellar microstructures. The FL γ/α_2 microstructure with randomly oriented lamellar colonies of 80 μm in size is shown in Fig. 1. A number of short rods of boride cross the lamellae can be seen.

The dimensions of specimens for various tests are shown in Fig. 2. Smooth flat tensile specimens were prepared with the dimensions as detailed in Fig. 2(a). Compression specimens have a 5×5 mm cross-section and are 12 mm in length as shown in Fig. 2(b). Specimens shown in Fig. 2(c)–(e) were used for in situ tensile tests and observations. The thickness of these specimens varies from 0.28 to 0.60 mm. Specimens were cut by electric-spark machining (ESM), mechanically polished through SiO_2 paper and then etched in a solution of 10% HNO_3, 3% HF and 97% water. The slit notch (S Notch) used for the in situ tensile specimen (Fig. 2(c)) was 1 mm in depth and 175 μm in width with a root radius of 87.5 μm. Fatigue tensile specimens, 3PB specimens and 4PB specimens for monotonic loading and fatigue loading were prepared with the dimensions as detailed in Fig. 2(f)–(i).
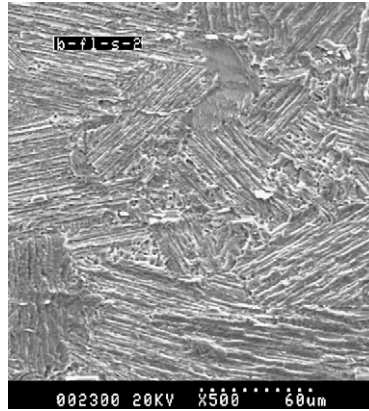
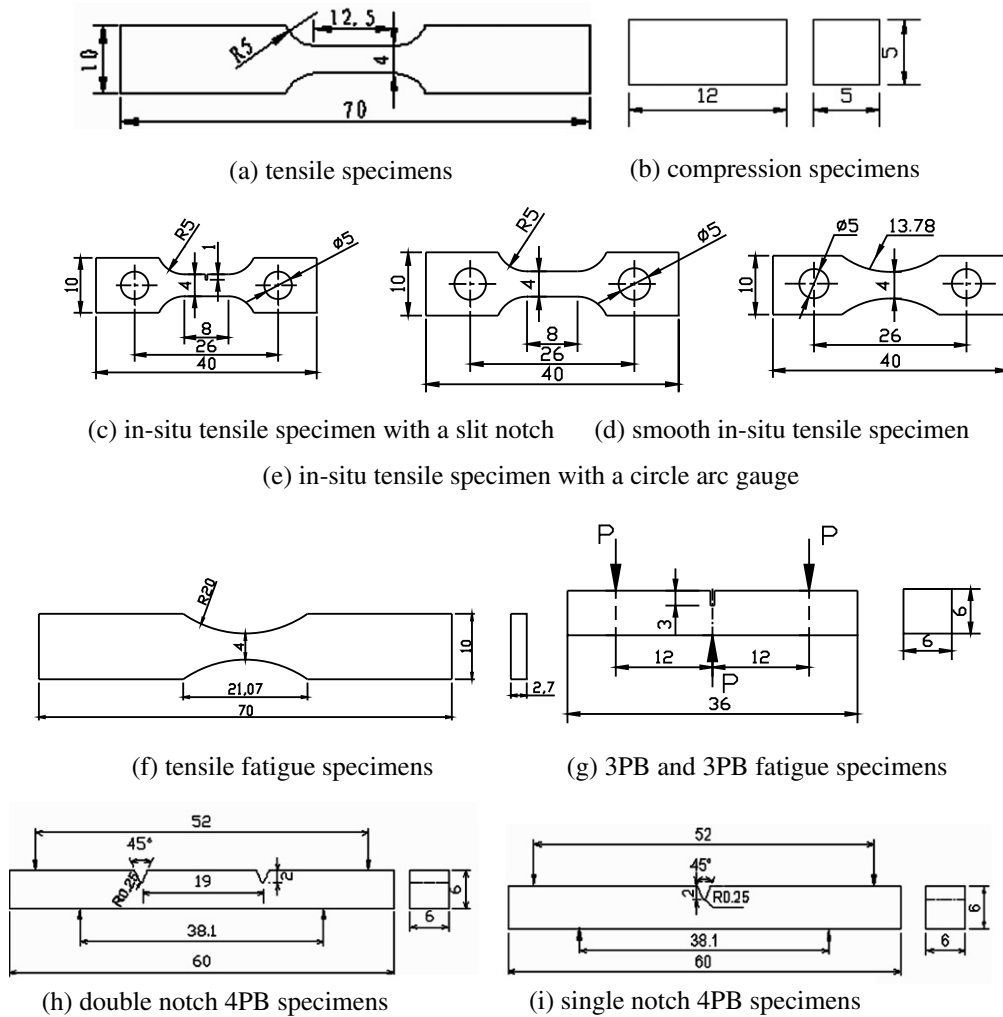Fig. 1. Microstructures of fully lamellar Ti–44Al–4Nb–4Hf–0.2Si–1B.

(a) tensile specimens

(b) compression specimens

(c) in-situ tensile specimen with a slit notch   (d) smooth in-situ tensile specimen

(e) in-situ tensile specimen with a circle arc gauge

(f) tensile fatigue specimens

(g) 3PB and 3PB fatigue specimens

(h) double notch 4PB specimens

(i) single notch 4PB specimens

Fig. 2. Shapes and dimensions of all specimens for various tests.

2.2. Tensile test

Tensile test was conducted at room temperature in an INSTRON 1341 test machine and were carried out at a crosshead speed of 0.025 mm/min. The yield stress ($\sigma_{0.2}$), ultimate tensile strength (σ_{uts}), fracture strain (ε_f), fracture stress (σ_f) and elastic modulus (E) were measured from engineering stress–strain curves.

Several tensile test specimens were unloaded at 266.6, 475.3 and 592.9 N prior to fracture. Two side surfaces parallel to the tensile direction of the specimens were polished after unloading and slightly etched, in order to observe microcracks on the surfaces produced prior to fracture.

2.3. Compression test

Compression test was conducted in air at room temperature in SHIMADSU AG-10TA universal test machine with at a cross-head speed of 0.025 mm/min. The yield stress $\sigma_{0.2}$, ultimate compression strength σ_{ucs}, total fracture strain ε_f and fracture stress σ_f were measured from engineering stress–strain curves. All values of applied stresses are defined as the corresponding loads divided by the original cross-section areas. Seven specimens were unloaded at stresses of 404.8, 600.0, 813.0, 1138.2, 1350.7, 1592.0 and 1995.5 MPa, respectively. Two side surfaces along the compression direction of the specimens were polished after unloading and slightly etched, in order to observe deformation and damage at various applied loads.

2.4. In situ tensile test

In situ tensile test was performed in vacuum using a calibrated loading stage in a scanning electron microscope (SEM) S-520. The specimens were slowly step-loaded manually. The crack patterns at various loading steps were recorded by SEM. Thus, the crack initiation and propagation processes in conjunction with applied loads were recorded.

2.5. Tensile fatigue test

Tensile fatigue test was conducted at room temperature in an INSTRON 1341 test machine at different stress amplitude values. Six different levels of the peak stress σ_{max} ranging from 378 to 511 MPa were applied, the R ratio was kept to $\sigma_{min}/\sigma_{max} = 0.1$. Some of specimens were tested to fracture and the others were unloaded at desired number of cycles prior to final fracture. Metallographic surfaces of these specimens were observed by SEM (JEOL-6700F). The frequency and fatigue life (the number of cycles) were recorded for tensile fatigue tests at each stress amplitude value.

2.6. Bending test under the monotonic loading mode

Three point bending (3PB) and four point bending (4PB) tests under the monotonic loading mode were carried out in air at room temperature in a SHIMADZU AG-10TA universal test machine with a cross-head speed of 0.5 mm/min. The fracture load P_f was measured directly from the load–displacement curve, and the energy (w_f) absorbed in fracture was measured by the area under the load–displacement curve. The values of K_{max} of fractured specimens in 3PB tests were calculated by following formulas:

$$S = 4W \quad \text{and} \quad K_{max} = \left(\frac{SP_{max}}{BW^{3/2}}\right)Y_{(a/w)},$$

$$Y_{(a/w)} = \left[\frac{3(a/w)^{1/2}\{1.99 - (a/w)(1 - a/w)[2.15 - 3.93(a/w) + 2.7(a/w)^2]\}}{2(1 + 2a/w)(1 - a/w)^{3/2}}\right].$$

Here, K_{max} is the maximum mode I stress intensity factor; W is the width of specimen; B is the thickness of specimen; a is the length of the slit notch; S is the span of loading; P_{max} is the maximum (fracture) load. Seven specimens were unloaded prior to the fracture at loads of 202, 389, 540, 690, 627, 706 and 890 N, respectively.

2.7. Bending fatigue test

Three point bending (3PB) fatigue test was conducted at room temperature in an EHF-FB05-4LA test machine at various stress amplitude values. The frequency and fatigue life were recorded. Some of specimens were tested to fracture and the others were unloaded at desired cycles to observe the microcracks produced prior to final fracture.

2.8. Observations of fracture surfaces and observations on the damage produced on side-surfaces of unloaded specimens

Observations were carried out on fracture surface of all fractured specimens by SEM JEOL-6700F. In addition to the general pattern of whole fracture surface, attention was focused on the cleavage initiation origins. Damages (microcracks, heavy deformation) produced on side-surfaces of unloaded specimens was observed by SEM JEOL-6700F.

3. Experimental results

3.1. Results of tensile and unloaded tensile tests

Table 1 shows the data measured for tensile test specimens. Fig. 3 shows curves plotting the applied stresses against the strains. The average apparent $\sigma_{0.2}$ is around 592.6 MPa. The average fracture stresses is 627.0 MPa, and the fracture strain is 0.803%. No appreciable stress-softening sector on the stress–strain curve appears before the final fracture. It means that it is fractured suddenly rather than fractured by crack propagation step-by-step. It is worth noting that Specimen B-T-01 shows a marked low value of 530.0 MPa of the fracture stress compared with that of other three specimens with an average value of 659.4 MPa.

Fig. 4 shows two typical fracture surfaces of tensile specimens. From Fig. 4(a)–(d) it was found that the final fracture of both specimens B-T-01 and B-T-05 was triggered by interlamellar cracks (enclosed by black

Table 1
Tensile results of fully lamellar Ti–44Al–4Nb–4Hf–0.2Si–1B

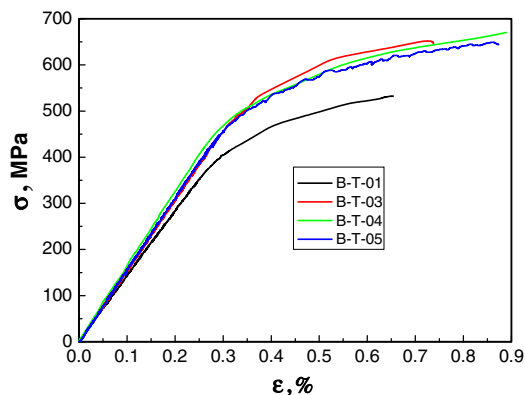| No.	S_e	E (GPa)	$\sigma_{0.2}$ (MPa)	ε_f (%)	σ_f (MPa)	σ_{UTS} (MPa)
B-T-01	4×1.63	141.5	523.7	0.66	530.0	532.5
B-T-03	4×1.96	153.6	639.7	0.74	632.6	652.0
B-T-04	4×1.94	161.9	593.0	0.94	670.5	670.5
B-T-05	4×1.92	157.3	613.9	0.87	679.6	679.6
Average		153.6	592.6	0.80	628.2	633.6

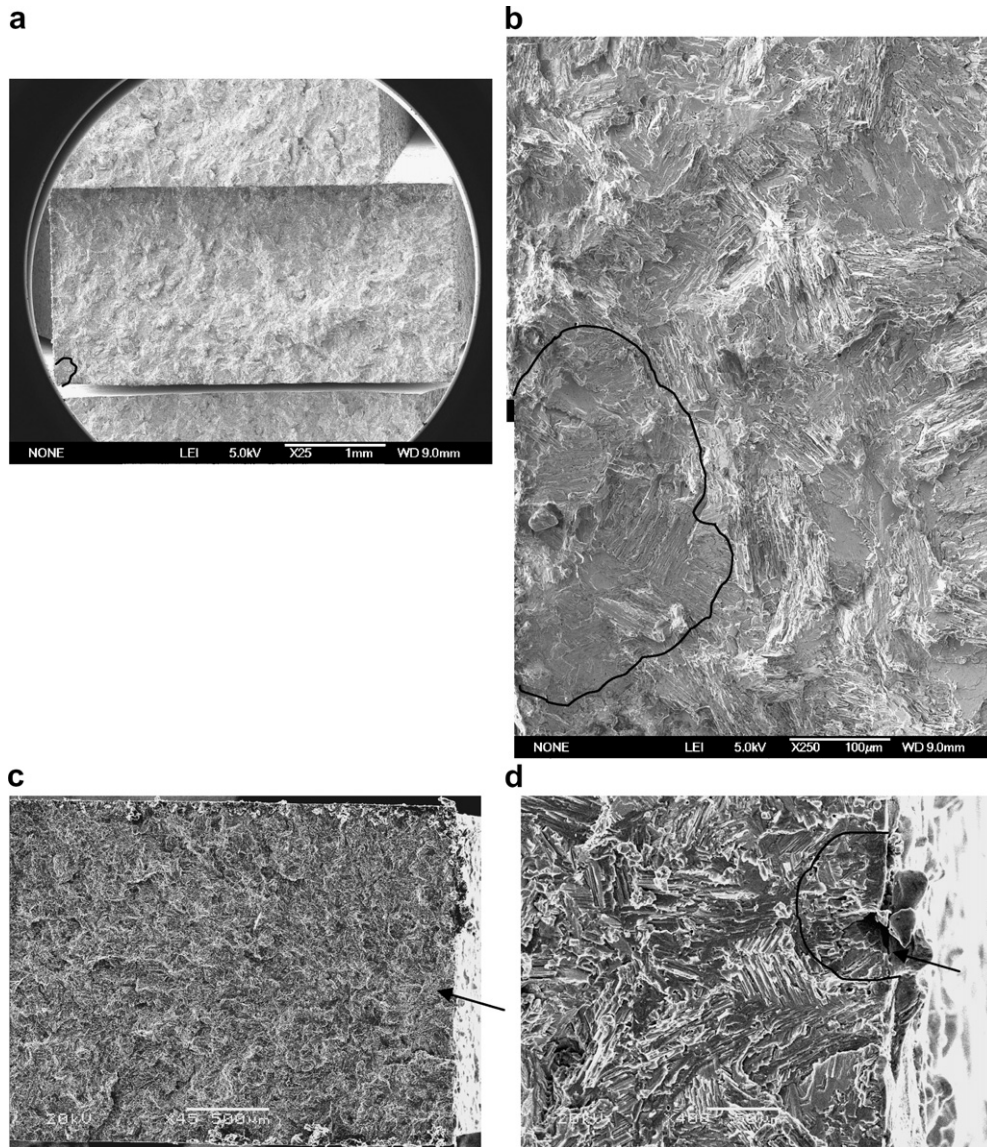Fig. 3. Tensile curves of fully lamellar Ti–44Al–4Nb–4Hf–0.2Si–1B.

Fig. 4. Fracture surface of tensile specimens. (a, b) Fracture surface of specimen B-T-01: (a) the black curve delineating the original critical crack and (b) a close view of the critical crack which triggered the cracking through the entire specimen. (c, d) Specimen B-T-05: (c) the black arrow showing the origin of cracking and (d) a close-up view of the original critical crack which triggered the cracking through the entire specimen.

curves) which extended to a critical length. For other two specimens B-T-03 and B-T-04, similar interlamellar cracks triggering the final fracture can be found. The lengths of these critical cracks in the direction of crack propagation for B-T-03, 04 and 05 specimens are in the range of around 80–100 μm, which is slight larger than the average grain size (lamellae colony size) of this alloy. Corresponding to the critical length of 80 μm the fracture stress is around 659.4 MPa. The surface energy calculated in line with the Griffiths formula is 356 J/m^2. Then the lower fracture stress measured in specimen B-T-01 can be attributed to its larger critical length of around 120 μm (Fig. 4(b)). It is consistent with the fracture mode suggested by the present authors [14,16] that when a microcrack extends to a critical length which matches the loading stress, the crack propagates catastrophically through entire specimen. This fracture mode is schematically drawn in Fig. 5(a). As discussed in [13,14], the present authors also suggested another fracture mode in tensile test that fracture
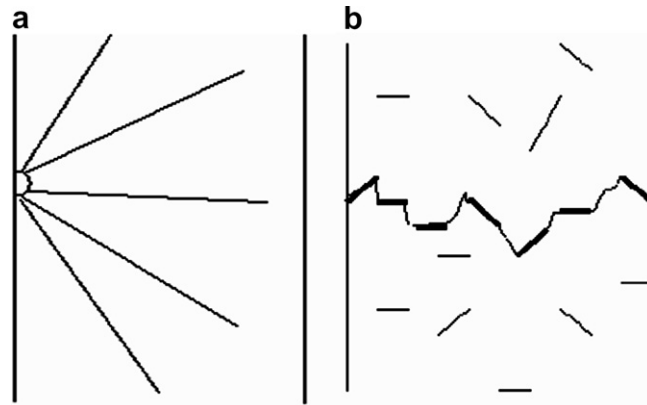
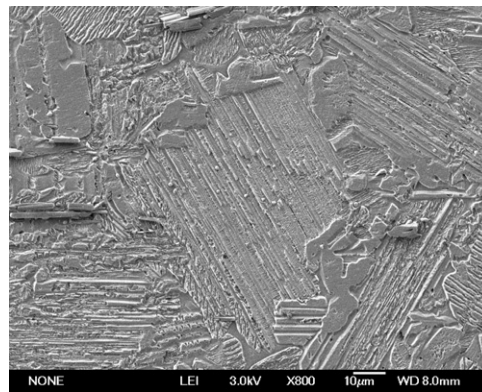Fig. 5. Schematic illustrations of two different fracture modes of tensile specimens.

Fig. 6. Metallographic surfaces of tensile specimens unloaded at 592.9 MPa.

occurs in the weakest section which is most heavily damaged by a number of large interlamellar microcracks. In large grain FL specimens, a great number of large interlamellar cracks are produced prior to final fracture. The final fracture happens in a section with the highest density of accumulated microcracks dividing the remaining region into separated small areas which break almost simultaneously (schematically shown in Fig. 5(b)). Because the section is severely weakened, the fracture stress is very low and shows a loading rate-dependent character. For the alloy investigated in this paper, the grain size is small and the interlamellar strength is high. The final fracture shows a critical crack-triggering mode. When the applied stress reaches a value matching that specified by a critical length (determined by the largest grain size) in line with the revised Griffiths formula, the fracture is triggered. Because sufficient energy has been accumulated in the loading process, once the critical length of a cleavage crack is reached, the specimen is fractured suddenly. Three specimens were unloaded at 266.6, 475.3 and 592.9 MPa prior to fracture. Fig. 6 shows a typical metallographic surface of specimen B-T-08 unloaded at 592.9 MPa. No remaining microcrack has been found on unloaded specimen surfaces. This fact supports the suddenly fracture mode suggested above.

3.2. Results of compression tests

The compression test results are listed in Table 2 and the compression curves are shown in Fig. 7. The average apparent $\sigma_{0.2}$ of this material in compression is 876.2 MPa. The average of the fracture stresses is 1932.2 MPa with an average fracture strain of 24.7%. A stress-softening sector (stress dropping with strain increasing) of the stress–strain curve appears before the final fracture, which means that cracks propagate

Table 2
Compression results of fully lamellar Ti–44Al–4Nb–4Hf–0.2Si–1B

| Type	No	Dimensions	$\sigma_{0.2}$ (MPa)	ε_f (%)	ε_u (%)	σ_f (MPa)	σ_u (MPa)	σ_{uts} (MPa)	W'_f (J/mm²)
Fractured specimens	B-C-201	4.97 × 4.88 × 12.06	851.1	26.0	–	2141.5	–	2242.5	0.054
	B-C-202	4.74 × 4.80 × 11.88	901.3	23.5	–	1722.9	–	2024.4	0.043
	Average		876.2	24.7	–	1932.2	–	2133.5	0.049
Unloaded specimens	B-C-203	4.88 × 4.96 × 11.98	–	–	1.5	–	404.8	–	–
	B-C-204	4.88 × 4.96 × 11.98	–	–	2.2	–	600.0	–	–
	B-C-205	4.82 × 5.00 × 12.00	–	–	2.8	–	813.0	–	–
	B-C-206	4.92 × 5.00 × 12.10	801.2	–	7.5	–	1138.2	–	–
	B-C-207	4.92 × 4.94 × 12.06	745.7	–	9.0	–	1350.7	–	–
	B-C-208	4.80 × 5.00 × 12.40	512.0	–	14.1	–	1592.0	–	–
	B-C-209	4.96 × 5.00 × 12.08	619.3	–	20.9	–	1995.5	–	–
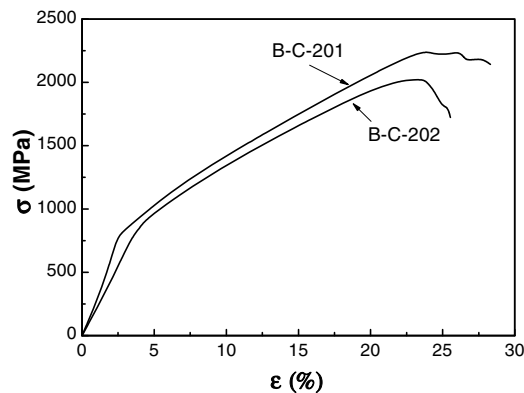
Fig. 7. Engineering stress–engineering strain curves of compression test.

step-by-step and then cause the final fracture. Comparing Tables 1 and 2, it can be found that all mechanical properties measured in compression are higher than those measured in tension. It is attributed to the difference of the deformation and fracture mechanisms between tensile tests and compression tests, which will be discussed later.

Fig. 8 shows the metallographs of surfaces of specimens (listed in Table 2) unloaded from 404.8, 600, 813.0, 1138.2, 11350.7, 1592 and 1995.5 MPa. At the applied stress lower than 600 MPa, no slip line appeared. When the applied stress was increased to 813.0 MPa, a few slip lines appeared, but no microcracks were found (Fig. 8(a)). At the applied stress of 1138.2 MPa, a few short cracks parallel or inclined to compressive loading direction appeared at boundaries of tortured grains or at interfaces between lamellae (Fig. 8(b)). With applied stress further increasing, more slip lines and extrusive (wedge in) ridges are observed and more interlamellar microcracks are found to be initiated and propagated along lamellar interfaces or at grain boundaries (Figs. 8(c) and (d)). It can be found that crack density and slip lines increase with increasing loading levels.

Based on the above microscopic observation in conjunction with the appearing of a stress-softening sector (stress dropping with strain increasing) in the stress–strain curve before the final fracture, it is inferred that in the compression specimens the final fracture occurs by extension of cracks step-by-step rather than a sudden crack triggering mode. The macroscopic fracture configuration shows that the final fracture is composed of several cracks parallel to the compressive load direction and/or cracks inclined with a small angle to it.

3.3. Results of in situ tensile tests

The results of in situ tensile test are listed in Table 3. Fig. 9 shows the in situ observation of surface crack propagation and the fracture surface of a slit-notched tensile specimen B-fl-s-10. As shown in Figs. 9(a) and (b), at an applied stress of around 260.7–299.1 MPa, crack 1 initiated along lamellar interfaces at the notch

(a) B-C-205   813 MPa

(b) B-C-206   1138 MPa

(c) B-C-208   1592 MPa
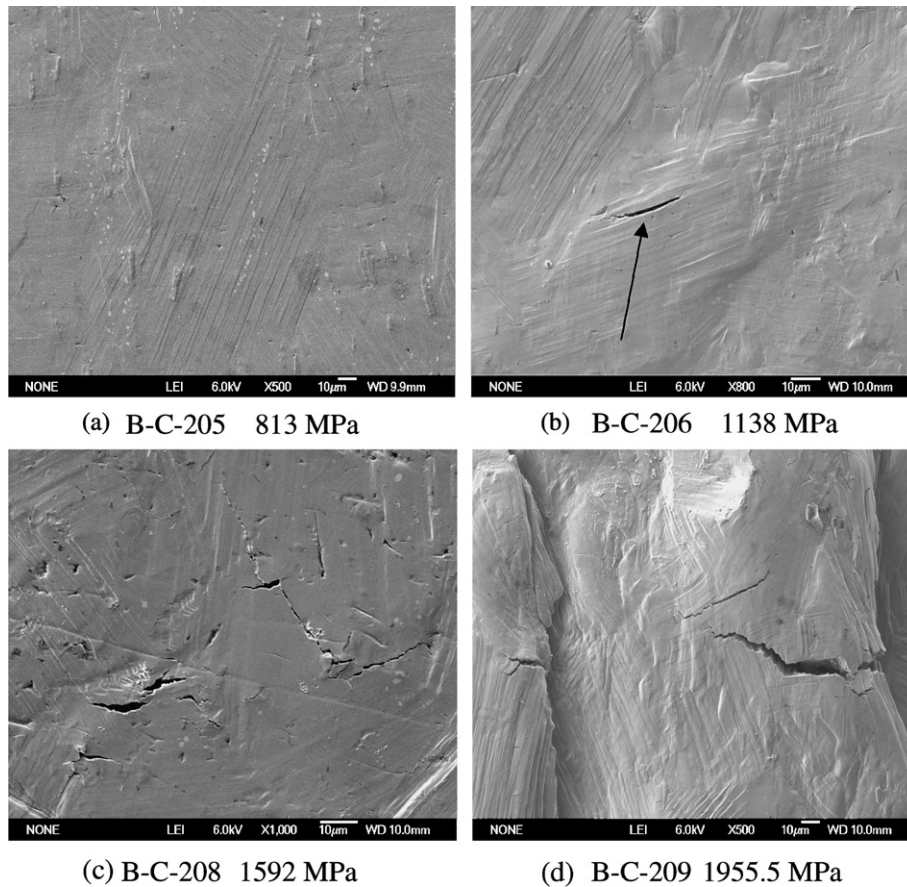
(d) B-C-209 1955.5 MPa

Fig. 8. Metallographic surfaces of compression specimens unloaded at indicated applied stress under each image. The compression axis is horizontal.

Table 3
In situ tensile results of fully lamellar Ti–44Al–4Nb–4Hf–0.2Si–1B

No.	Type	S_e (mm^2)	N	L_{max} (μm)	P_i (N)	σ_i (MPa)	P_f (N)	σ_f (MPa)
B-S-10	Slit-notched	0.58 × 3	3	200	454.0	260.9	815.4	468.6
B-S-07	Slit-notched	0.48 × 3	–	–	–	–	316.1	219.5
B-S-02	Big circle arc	0.34 × 3	5	250	398.0	390.2	401.8	393.9
B-S-19	Flat	0.28 × 3	4	60	585.6	697.1	640.4	762.4

root. Crack 2 and crack 3 initiated and propagated along lamellar interfaces at a distance around 50–100 μm ahead of the notch root, where the highest stress is located. With increasing the applied stress, the two cracks were connected with each other (Fig. 9(c)) and propagated both backward to notch root and forward (Fig. 9(d)). The advancing crack tip stopped at a barrier grain with lamellae oriented perpendicular to the crack as shown in Fig. 9(d) and (e). After the main crack had propagated through the barrier grain by translamellar cracking (with a length of 200 μm) at an applied stress of around 466.9 MPa, the specimen was fractured suddenly (Fig. 9(f)). Fig. 9(g) and (h), showing the fracture surface of this specimen, illustrates visually the cracking process observed during in situ tensile tests. Corresponding to the interlamellar crack 2 and 3 in Fig. 9(a) and (b), a large interlamellar crack facet was found and is shown in Fig. 9(g). The translamellar propagation of the main crack in Fig. 9(d) and (e) also corresponds to a translamellar crack facet in the middle part of Fig. 9(h). Once a crack with a critical length is produced under the normal stress intensified by the slit
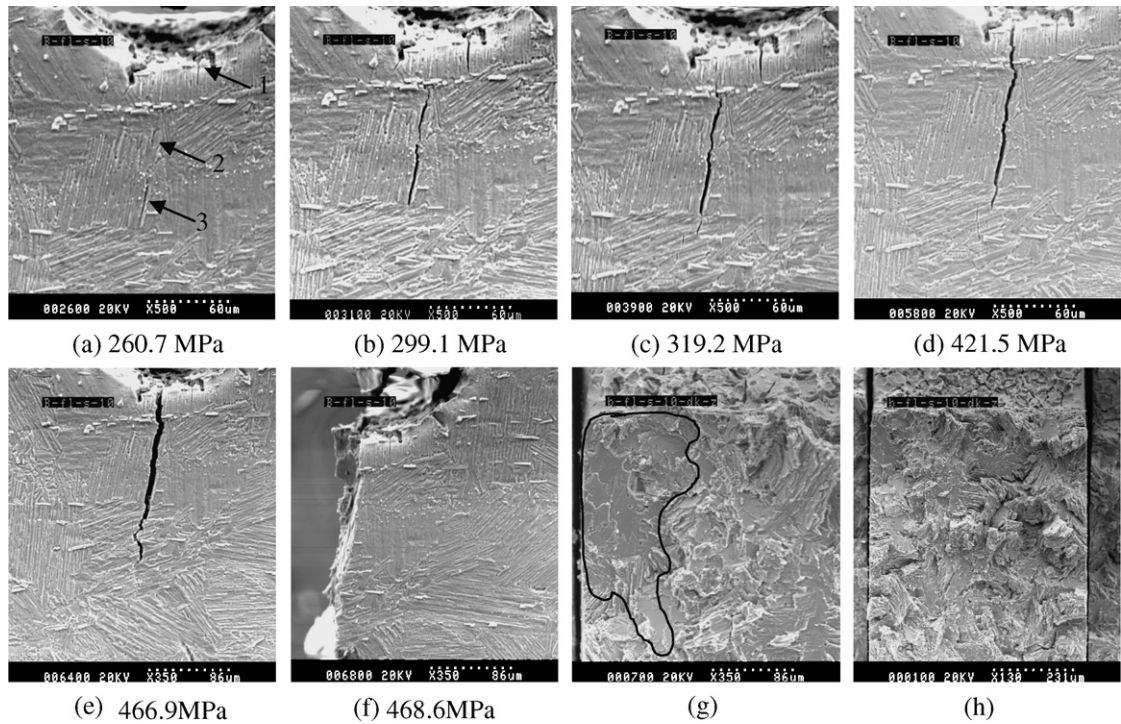
Fig. 9. Crack evolution observed at surface of slit-notched tensile specimen B-s-10 at different stress levels (a–f) and corresponding fracture surface of a slit-notched tensile specimen B-s-10 (g, h).

notch, the final fracture of the entire specimen occurs suddenly. Fig. 10 shows a typical cleavage fracture surface of specimen B-fl-s-07 with a slit notch, where the final fracture was also triggered by an interlamellar crack. The main crack propagated forward through a number of facets with distinct directional cleavage traces. This is a general picture of the fracture surface for a notched TiAl specimen fractured in tension. In many cases, it was found that the interlamellar cracks were blocked by boride rods as clearly shown in Fig. 18(b), which shows beneficial effects to the interlamellar strength.

For smooth in situ tensile specimen (Fig. 2(d)) or those with a large arc gauge (Fig. 2(e)) such as B-fl-s-19 and B-fl-s-2, a number of interlamellar microcracks were produced in the ligament of the specimen at the
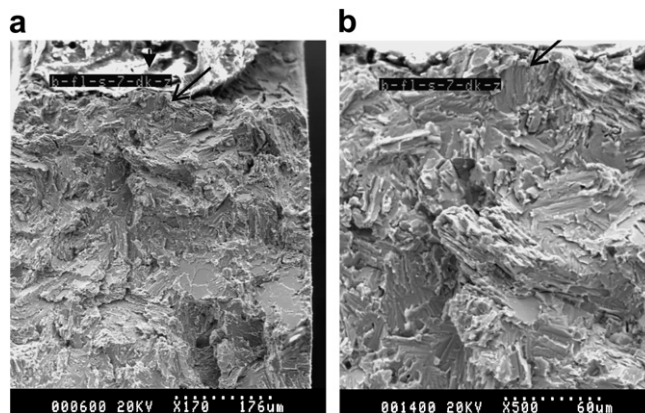

Fig. 10. Fracture surfaces of in situ slit notch tensile specimen B-s-7. (a) A general view, the black arrow shows the origin of cracking and (b) a close-up view of the original critical crack which triggered cracking through the entire specimen.
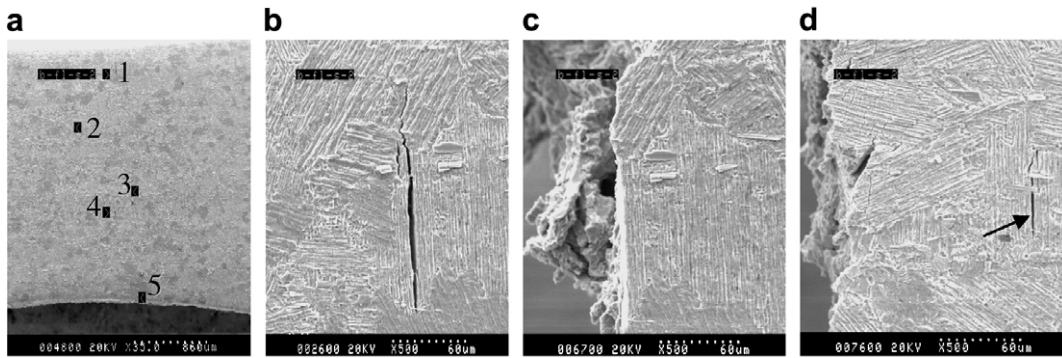
Fig. 11. Surface crack configuration before and after fracturing for a big arc in situ tensile specimen B-s-2. (a) A general view showing five surface cracks, (b) a close-up view of crack 1, (c) crack 1 after fracture and (d) the arrow showing the crack 3 after fracture.

applied stress around 350–390 MPa as shown by arrows 1, 2, 3, 4, 5 in Fig. 11(a). The magnified crack 1 is shown in Fig. 11(b). Fig. 11(c) shows its configuration after fracture. The final fracture happened suddenly and the main crack passed through four cracks (crack 1, 2, 4, 5) observed in situ tensile test (figure during testing (Fig. 11(a)). Fig. 11(d) shows the remaining crack 3, which was not involved in the final fracture path. Because in these specimens there were no artificial stress intensifiers such as a slit notches or precracks, the produced microcracks were distributed randomly over the entire ligament. And because these specimens were very thin (0.28–0.60 mm in thickness), the final fracture in a relative long ligament could not be triggered by a single interlamellar crack as that happened in flat specimens in tensile tests. From the observations of the fracture surfaces, it is considered that the final fracture was triggered by the connection of microcracks like those found in Fig. 11.

3.4. Results of bending tests under the monotonic loading mode

Table 4 shows the results of 3PB bending tests using slit notched specimens and Fig. 12 shows the applied load–displacement curves. No stress-softening sector (load dropping with displacement increasing) in the load–displacement curve appears before the final fracture. It means that it was fractured suddenly rather than fractured by step-by-step crack propagation. Comparing the values of K_{max} of the fine grain specimens in this study with that of a coarse grained specimen ($\sim$1000 μm in colony size) in [14], as shown in Table 5, it is interesting to find that even though the characteristic values measured in tensile tests, such as the fracture stress and fracture strain of the finer FL specimens are remarkably superior to those of coarse FL specimens, the K_{max} of the fine grain specimens are lower than that of coarse grain specimens. These results support the argument that tensile ductility and fracture toughness depend upon colony or grain sizes in opposite ways [15,17,18]. The explanation of this phenomenon was given in the author's previous papers [14,15] and will be illustrated again later.

Fig. 13 shows the fracture surface of specimen 3PB-301 (Table 4). A cleavage origin was found at a distance of 70 μm from the root of the slit notch (shown in Fig. 13(a)). In the close-up viewing picture in Fig. 13(b), the cleavage origin was formed by an interlamellar crack-dominant facet 80 μm in size. Similar feature was also found on the fracture surface of a 4PB specimen: the cleavage fracture was triggered by an interlamellar crack 50 μm in size and 130 μm from the root of the V-notch.

Table 4
Bending test results of fully lamellar Ti–44Al–4Nb–4Hf–0.2Si–1B

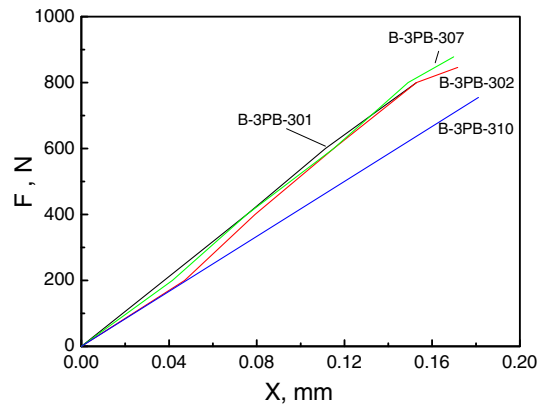| No.	W (mm)	B (mm)	a (mm)	a/W	P_{max} (N)	w' (J/mm^2)	K_{max} (MPa m$^{1/2}$)
B-3PB-301	6.00	6.02	2.856	0.476	800.0	3.280×10^{-3}	16.96
B-3PB-302	5.98	6.00	2.808	0.470	846.0	3.899×10^{-3}	17.75
B-3PB-307	5.98	6.04	2.851	0.477	878.0	3.986×10^{-3}	18.70
B-3PB-310	5.96	5.96	2.820	0.473	755.0	3.654×10^{-3}	16.18
Average					819.8	3.705×10^{-3}	17.40

Fig. 12. Displacement–load curves of 3PB bending test.

Table 5
Comparison of properties of fine grain FL Ti–44Al–4Nb–4Hf–0.2Si–1B and a coarse grain FL TiAl alloy

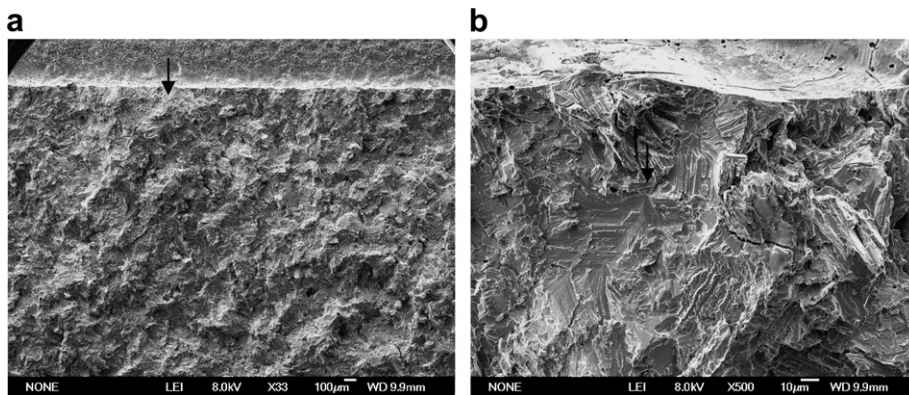| No.	$\sigma_{0.2}$ (MPa)	ε_f (%)	σ_f (MPa)	σ_{UTS} (MPa)	P_{max} (N)	K_{max} (MPa m$^{1/2}$)
Fine grain FL microstructures	592.6	0.80	627.0	633.6	819.8	17.40
Coarse grain FL [14]	–	0.261	236.7	236.7	1110.2	22.60

Fig. 13. Fracture surface of specimen B-3PB-301 after 3PB test. (a) A general view, the blank arrow showing the origin of cracking and (b) a close-up view of the original critical crack which triggered cracking through the entire specimen.

These results are similar to those revealed for fine grain duplex phase TiAl alloys in [14]. Based on the results of measured load–displacement curves and microscopic observations, it is concluded that the fracture mechanism of notched bending specimen of fine grain FL TiAl is critical crack-triggered cleavage, rather than step-by-step crack propagation observed in a very large FL microstructure. This fracture mode is just like what happens in HSLA steel tested at low temperature.

Even though in unloaded 3PB specimens, a number of microscopic surface cracks were observed, due to their short length and shallow depth the effects of these microcracks can be neglected.

3.5. Results of tensile fatigue tests

The tensile fatigue results are listed in Table 6. Following the general rule for fatigue fracture, the fatigue life decreases with increasing the load amplitude. Figs. 14(a) and (b) shows the fracture surfaces of specimen

Table 6
Tensile fatigue results of fully lamellar Ti–44Al–4Nb–4Hf–0.2Si–1B

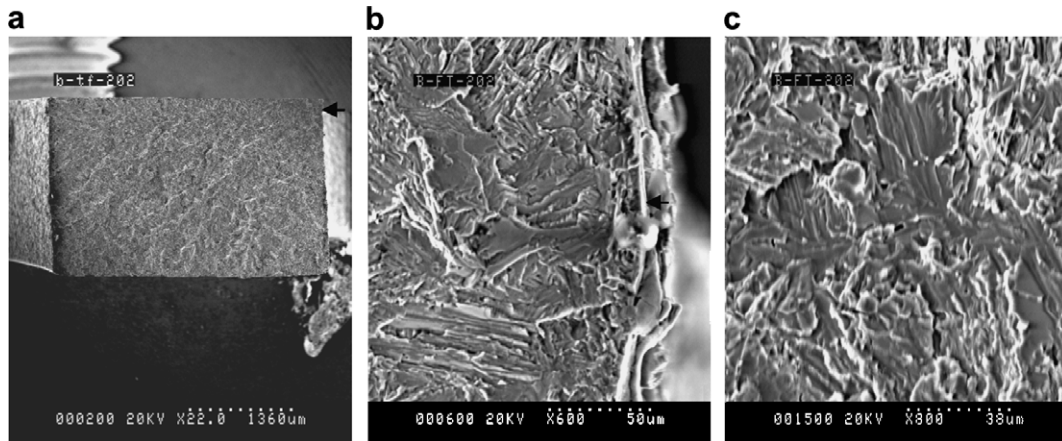| No.	B (mm)	σ_{max} (MPa)	σ_a (MPa)	σ_m (MPa)	f	N_f	N_u
B-TF-201	2.6	420	189.0	231.0	30	61388	
B-TF-202	2.57	390	175.5	214.5	30	105286	
B-TF-203	2.49	360	162.0	198.0	30		1234560
B-TF-204	2.52	378	170.1	207.9	30	318675	
B-TF-205	2.51	378	170.1	207.9	30		286808
B-TF-206	2.54	378	170.1	207.9	30		191205

Fig. 14. Fracture surface of tensile fatigue specimen B-TF-202. (a) A general view, the black arrow shows the origin of cracking and (b, c) close-up views of the crack origin which is a cluster consisting of several interlamellar cracks connected by translamellar cracking.

B2-TF-202, a specimen fractured at $\sigma_{max} = 390$ MPa, $\sigma_{min} = 39$ MPa and $N_f = 105286$. It is apparent that the final fracture was caused by the propagation of the main cleavage crack triggered by a cluster of cracks located at the upper right corner (Fig. 14(a)). This crack cluster consists of several interlamellar cracks which are connected by translamellar cracks and extends to a length of around 180 μm in the direction of the main crack propagation (Fig. 14(b)). The other four tensile fatigue fractured specimens show the same fracture behaviour, each with a cluster of cracks triggering the final catastrophic cleavage fracture. The crack clusters also consist of several interlamellar cracks, which are connected by translamellar cracks and located at various sites. The only remaining surface crack was observed in the specimen unloaded at 378 MPa and 286,808 cycles (B-TF-205 in Table 6) as shown in Fig. 15. Then it is considered that in most cases the original crack is initiated at a distance from the surface where the stress is higher due to the stress intensification caused by the specimen configuration with an arc-shape gauge (Fig. 2(f)).

From above observations, the fracture mechanism of tensile fatigue tested specimens can be summarized as that under tensile fatigue loading, at a highly stressed site, several interlamellar cracks successively initiate, propagate and connect each other through translamellar cracking. Once the length of a cluster of cracks matches the applied stress and reaches the critical length, the cleavage crack propagates catastrophically through the entire specimen. The higher the applied maximum stress, the shorter the necessary critical length of the crack cluster which triggers the final fracture. In specimen B2-TF-02, the crack cluster length reaches 180 μm which is much larger than that of 80 μm observed in monotonic tensile tested specimen, and correspondingly the fatigue maximum tensile stress of 390 MPa is much lower than 627 MPa of the average monotonic tensile fracture stress. With decreasing the maximum applied stress (i.e., the fatigue stress amplitude), the necessary length of the crack cluster increases and the number of the fatigue cycles to produce it increases. As long as the maximum applied stress (i.e., the fatigue stress amplitude) is lower than the value that could produce a crack cluster with a length matching the stress, the specimen will not fail.
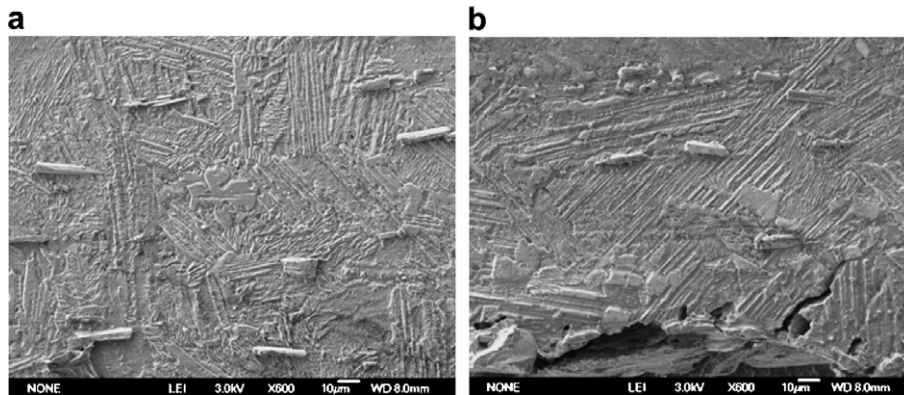
Fig. 15. Metallographic surfaces of fatigue tensile specimen B-TF-205 unloaded at the cycle number of 286808.

3.6. Results of bending fatigue tests

Table 7 shows the results of bending fatigue test. Fig. 16 shows the side surface view of the main cracks near the notch roots in specimens that were unloaded at desired cycles under nearly constant load amplitude. It was found that the fatigue crack initiates at the notch root and extends preferentially along interfaces between lamellae, as shown by arrow 1 in Fig. 16(b) and (h). When the crack propagates to the boundary of another lamellar colony with different orientation, the fatigue crack deflects and propagates along grain boundaries (marked by arrows 2 in Fig. 16(f)) or along interfaces between lamellae in another grain (marked by arrows 3 in Fig. 16(i)). Fig. 17 shows the plot of fatigue crack lengths measured on the two side surfaces of unloading specimens against the fatigue cycles under a nominal maximum stress $\sigma_{\mathrm{max-n}}$ around 20 MPa. The crack length increases with increasing fatigue cycle except for the data from the last specimen with a high fatigue cycle. These odd points are from specimen B-F-3PB-027, of which the configuration of the crack is shown in Fig. 18. It can be seen that in the vicinity of the notch root there are many boride rods perpendicular to the crack direction. It is apparent that these boride particles provide the extra-resistance to the crack propagation and make the crack length shorter during the fatigue loading process. Fig. 16 also shows the toughening mechanism mentioned in [15], such as blunting of the crack tip (in Fig. 16(c) and (i)), deflection of crack by lamellae (in Fig. 16(b) and (e)) and bifurcation of crack (in Fig. 16(e)).

From Table 7, it is found that with decreasing applied stress amplitude, fatigue life also increases. Different applied stress amplitudes also lead to the different features of fracture surface. Fig. 19 shows the fracture surfaces of specimens fractured at the lowest and the highest maximum nominal stresses $\sigma_{\mathrm{max-n}}$ around 19.46 and 26.56 MPa with the highest and the lowest fatigue cycles of 554,400 and 23,900, respectively. The fracture sur-

Table 7
Bending fatigue results of fully lamellar Ti–44Al–4Nb–4Hf–0.2Si–1B

| No.	W (mm)	B (mm)	a (mm)	a/W	S_{e} (mm^2)	$\sigma_{\mathrm{max-n}}$ (MPa)	N_{f}	N_{u}
B-F-3PB-012	5.98	5.98	2.83	0.47	18.83	26.56	23,900	
B-F-3PB-014	5.98	6.02	2.87	0.48	18.71	21.38	83,600	
B-F-3PB-016	6.02	6.00	2.81	0.47	19.27	19.46	554,400	
B-F-3PB-020	6.04	5.98	2.84	0.47	19.11	20.14	235,400	
B-F-3PB-021	6.02	6.04	2.86	0.47	18.37	20.14	306,900	
B-F-3PB-025	5.98	5.74	2.93	0.49	17.59	20.18	457,400	
B-F-3PB-026	5.96	5.82	2.85	0.48	18.38	20.13	343,000	
B-F-3PB-027	5.96	5.82	2.85	0.48	18.27	20.25		330,400
B-F-3PB-029	6.00	5.84	2.94	0.49	16.8	20.23		289,300
B-F-3PB-030	6.04	5.83	2.82	0.47	18.51	20.26		254,600
B-F-3PB-033	6.00	5.81	2.89	0.48	17.87	20.14		216,600
B-F-3PB-024	5.98	6.04	2.89	0.48	18.17	20.09		183,800
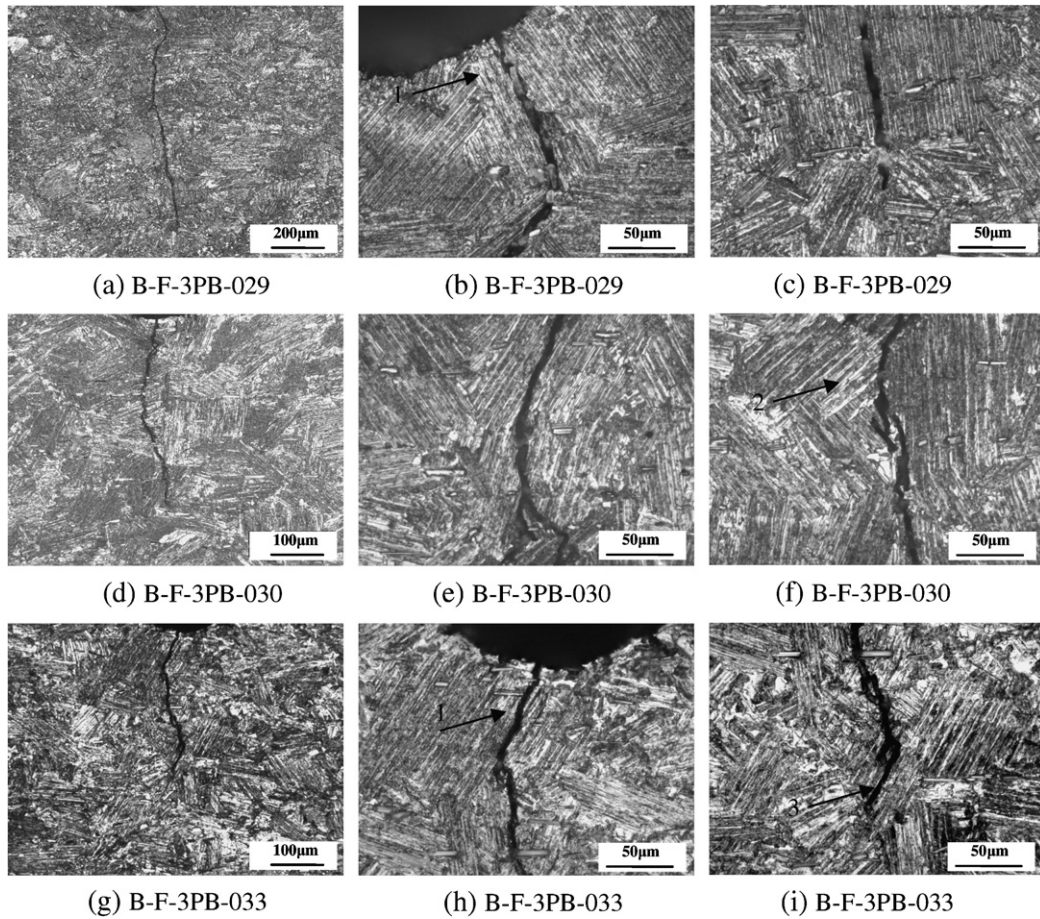
Fig. 16. Metallographic surfaces of the notch roots of 3PB fatigue specimens unloaded after different fatigue cycles with nearly same stress amplitude $\sigma_{\text{max}-n}$ of around 20 MPa. (a–c) Specimen B-F-3PB-029, $Nu = 289,300$, (d–f) specimen B-F-3PB-030, $Nu = 254,600$, (g–i) specimen B-F-3PB-033, $Nu = 216,600$.
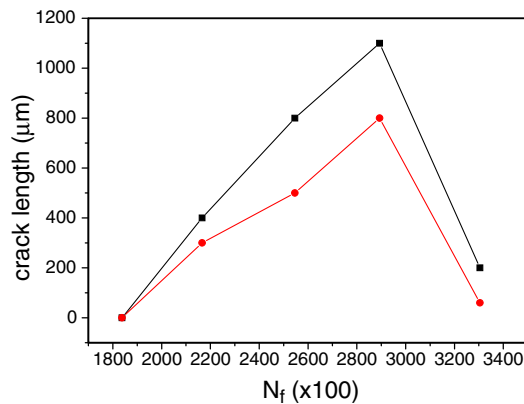

Fig. 17. Fatigue crack length vs. loading cycles at a nearly same maximum stress amplitude $\sigma_{\text{max}-n}$ of about 20 MPa.

face of the specimen B-3PB-F-016 fractured at $\sigma_{\text{max}-n} = 19.46$ MPa shows much more and larger interlamellar crack facets than that shown on the fracture surface of specimen B-3PB-F-012 fractured at $\sigma_{\text{max}-n} = 26.56$ MPa. It is consistent with the typical step-by-step propagation process of a fatigue crack
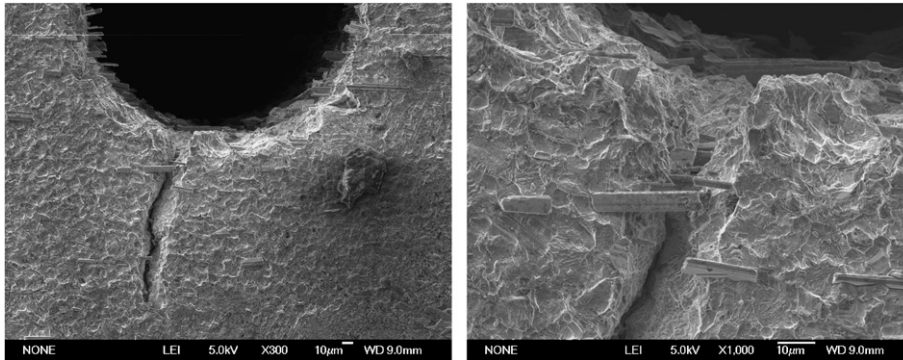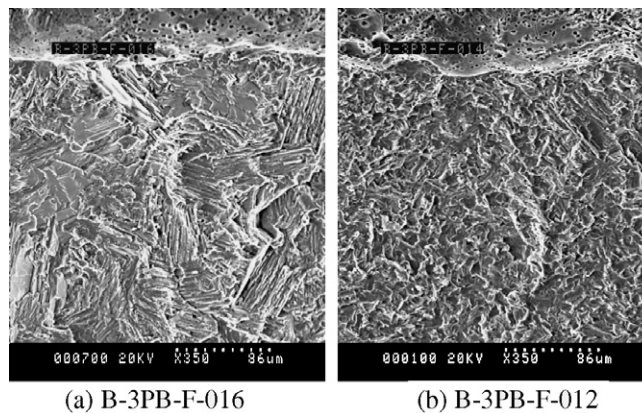
Fig. 18. Metallographic surfaces of 3PB fatigue specimens B-F-3PB-027 unloaded after 330,400 fatigue cycles.

(a) B-3PB-F-016   (b) B-3PB-F-012

Fig. 19. Fracture surfaces of (a) specimen B-3PB-F-016 fractured at lowest maximum fatigue nominal stress σ_{max-n} of 19.46 MPa and (b) specimen B-3PB-F-012 fractured at highest maximum fatigue nominal stress σ_{max-n} of 26.56 MPa.

described in Fig. 16. However, the fracture surface of the specimen B-3PB-F-012 fractured at high σ_{max-n} is relatively smooth. No typical interlamellar fracture and translamellar fracture facets for TiAl alloys are apparent, and the boundaries of grain and lamellar colony are not obvious. This fracture shows the mechanism for a fast propagating fatigue crack under a higher cyclic load.

In summary, for the normal fatigue fracture, the fatigue crack initiates directly at the notch root then extends step-by-step through the entire specimen under bending fatigue loading. Or the specimen is cleavage-fractured due to the reduction of ligament caused by the extension of the fatigue crack. No physical boundaries and no feature difference between the fatigue cracks and the cleavage cracks could be recognized. This fracture behaviour is different from that observed above in tensile, tensile fatigue and bending tests, during which a cleavage crack nucleus always initiates, then extends to a critical length and triggers the catastrophically propagation towards the rest of the ligament.

4. Discussion

Based on the observations described above, it is found that the fracture behaviour of TiAl alloy are different under various loading modes. It is discussed as follows.

4.1. Tensile test versus compression test

The fracture stresses measured in tension are much lower than those measured in compression. Most cracks propagate along the lamellar interfaces perpendicular or inclined with a large angle to the tensile direction.

Apparently, cracking is driven by the tensile stress along the weakest interfaces. In compression, crack may be driven by the tensile stresses perpendicularly to the compressive axis (cleavage crack parallel to the compressive axis) or driven by the shear stress (tearing crack inclined to the compressive with an angle close to 45°). In both cases the driving stress is much lower comparing to the case of the tensile test at same load. Thus, a larger applied load is needed to propagate the crack and results in a higher fracture stress. The reason of the early deviation of the stress–strain curves from the elastic straight line in the tensile tests (non-elastic strain occurs much earlier) is considered to be caused by the volumetric effects of the produced microcracks, which has been revealed in [13].

4.2. Smooth specimen versus notched specimen

In notched specimens (in situ tensile, monotonic tensile, monotonic bending), an interlamellar crack initiates and extends in front of the notch where the stress is intensified to a higher value. In most cases, the crack extends inside a lamellar colony and reaches the full size of the colony. When the applied load reaches the fracture load which produces a critical stress matching the size of the critical crack, the crack propagates through entire specimen (as schematically illustrated in Fig. 5(a)). In smooth specimen or specimen with a large arc gauge where there is no stress intensifier, interlamellar microcracks initiate and extend randomly in the ligament of specimen, and the final fracture proceeds by connection of microcracks through translamellar cracking (as schematically illustrated in Fig. 5(b)).

4.3. Monotonic loading versus cyclic loading

For fatigue test, the final fracture may be triggered by a critical crack cluster and developed by a sudden cleavage or by step-by-step crack propagation. In the former case, due to the low fatigue load (compared to the high monotonic load), a larger critical crack cluster is needed and produced by connecting several interlamellar cracks under repeated action of the cyclic loading. The difference between the fractures caused by the monotonic loading and cyclic loading lies in the different sizes of the critical cracks and its components (single interlamellar crack versus crack cluster composed of interlamellar crack with translamellar crack ridge). The lower the applied fatigue load, the larger the critical crack needed and the longer the fatigue life (cyclic number). In the latter case, which occurs in notched specimen, the final fracture is carried out by the step-by-step propagation of the crack driven by the fatigue tensile stress intensified by the notch. Because the frontier of a constant stress in a field produced by a notch moves forward only with the increase in the applied load, an R curve showing an increase in stress intensity against the increase in crack length can be measured. Till the reduction in the ligament area makes up the necessary increment of applied stress the applied load decreases.

4.4. High tensile properties versus lower fracture toughness

The fine grain high strength TiAl alloy investigated in this paper shows a fracture toughness lower than that of a previous investigated TiAl alloy with much larger grain and much lower strength (Table 5). The reason why a coarse TiAl alloy showing high fracture toughness has been investigated in previous paper and schematically illustrated as follows. In tensile test, the final fracture in FL specimens happens in a weakest section, which is heavily damaged by many very large lamellar cracks (~1000 μm). This weakest section could be located at any position within the gauge volume. In the small grain sizes, even in the weakest section the damage induced by microcracks is lighter than that induced in coarse grain FL specimens. Combined with the effect of fine grains, the lighter damage makes the fine grain FL specimen stronger than the coarse grain FL specimen in tension. The key factor is that in a tensile test specimen fracture can occur in a weakest section that could be located at any position in a large sampling volume (within all gauge regions). However, in the 3PB test, the propagation of the main crack is limited to a narrow strip nearby the centerline of the notch tip. Although the crack prefers to take a low resistance way through interlamellar cracks in some sites, yet the chances are limited by the narrow strip for propagation. Therefore, even at the lowest loading rate, the areas occupied by interlamellar cracks are much less in 3PB tested specimens (Fig. 20(a)) than in tensile tested specimens of coarse grain FL alloys (Fig. 20(b)).
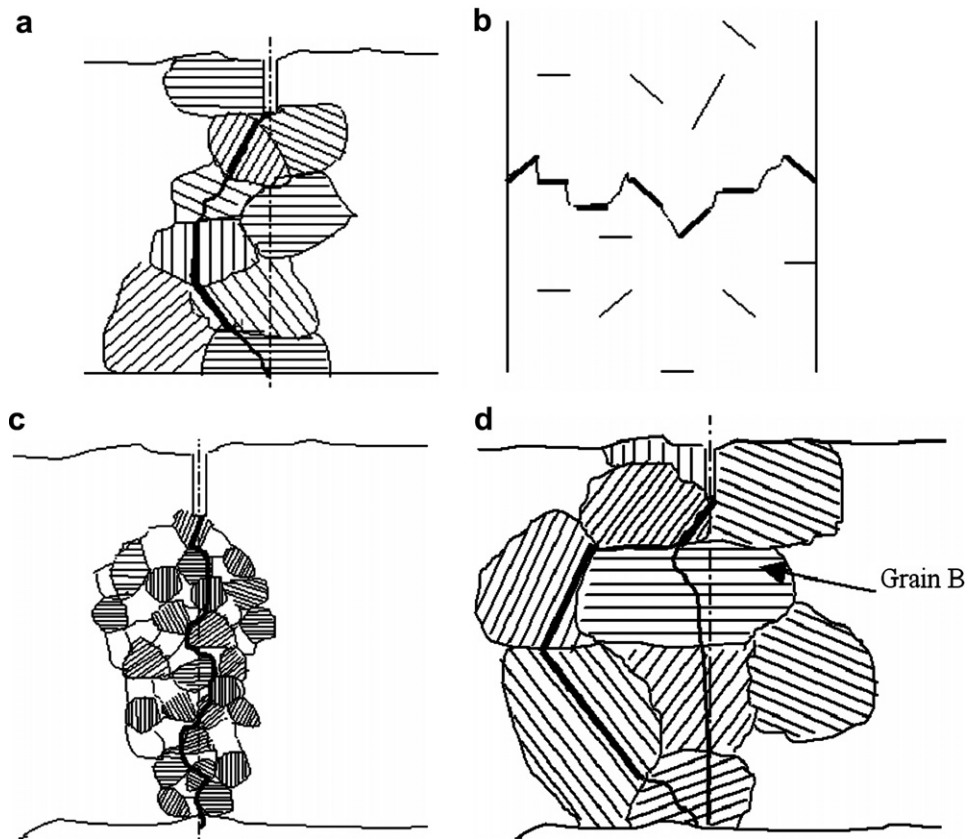
Fig. 20. Schematic illustrations showing crack propagation paths of FL microstructure in (a) 3PB specimen at low loading rate, (b) tensile specimens, (c) fine grain 3PB specimens and (d) coarse grain 3PB specimens.

In fine grain FL specimens even within a narrow strip the main crack can propagate through more interlamellar cracks by bypassing small grains with non-favorite orientation as schematically shown in Fig. 20(c). However, in coarse grain FL specimens, the main crack prefers to take the way through translamellar cracking rather than to bypass a very large grain (grain B) with non-favorite orientation (schematic in Fig. 20(d)), which results in the small quantity of interlamellar crack facets on the fracture surface of specimens fractured and a higher fracture toughness.

5. Conclusions

The fracture mechanisms of the FL TiAl alloys under various loading modes can be summarized as:

(1) Cracks initiate at grain boundaries and/or interfaces between lamellae.
(2) When a crack extends to a critical length which matches the loading stress the crack propagates catastrophically through entire specimen.
(3) The critical crack is produced suddenly by the applied loading in the monotonic tensile and bending tests.
(4) Fatigue cracks are initiated from the notch root, then extended step-by-step by the fatigue loads. For bending fatigue test, the fatigue cracks are initiated and extended directly from the notch root and propagate step-by-step through entire specimen at a lower fatigue load. For tensile fatigue test, the fatigue cracks reach their critical length and trigger the cleavage at a higher load and cause the final fracture of the whole specimen.

(5) In compression test, cracks initiate and propagate in directions parallel (driven by the tensile stress) or inclined to the compressive load (driven by the shear stress) after an appreciable plastic strain. Specimens are fractured by the propagation of cracks in both directions.

Acknowledgements

References

[1] Kim YW, Dimiduk DM. In: Chan KS, editor. Proceedings of George R. Irwin symposium on cleavage fracture. The Minerals, Metals & Materials Society; 1997. p. 305–17.
[2] Inui H, Oh MH, Nakamura A, Yamakuchi M. Room-temperature tensile deformation of polysynthetically twinned (PST) crystals of TiAl. Acta Mater 1992;40(11):3095–104.
[3] Akiyama, Yokoshima S. Johnson DR. Kishida K. Yamakuchi M. In: Chan KS, editor. Proceedings of George R. Irwin symposium on cleavage fracture. The Minerals, Metals & Materials Society; 1997. p. 293–303.
[4] Trail SJ, Bowen P. Effect of stress concentrations on the fatigue life of a gamma-based TiAl. Mater Sci Engng A 1995;192/193:427–34.
[5] Halford TP, Bowen P. The effect of single and multiple overloads on the fatigue crack growth of high strength titanium aluminides. J Mater Process Technol 2004;153–154:615–21.
[6] Gilbert He'naff*, Anne-Lise Gloanec. Fatigue properties of TiAl alloys. Intermetallics 2005(13):543–58.
[7] Francesco M, Rebuffo A, Sorrentino F. Effects of low-cycle fatigue on bending properties and fracture toughness of un-HIP'ed Ti–47Al–2Cr–2Nb–1B intermetallic. Int J Fatigue 2005(27):143–53.
[8] Gloanec AL, Henaff G, Betheace D, et al. Fatigue crack growth behavior of a γ-titanium–aluminide alloy prepared by casting and powder metallurgy. Scr Mater 2003(49):825–30.
[9] Chan KS. The fracture resistance of a binary TiAl alloy. Metall Mater Trans A 2000;31(2):71–80.
[10] Wang P, Bhate N, Chan KS, Kumar KS. Acta Mater 2003;51:1573–91.
[11] Chen JH, Cao R, Wang GZ, Zhang J. Study on notch fracture of TiAl alloys at room temperature. Metall Mater Trans A 2004;35(2):439–57.
[12] Hazzledine PM, Kad BK. Yield and fracture of lamellar γ/α_2 TiAl alloys. Mater Sci Engng A 1995;192/193:340–6.
[13] Cao R, Zhu H, Chen JH, Zhang J, Yao HJ. Effects of microcrack-damage on fracture behavior of TiAl alloy – Part I. Displacement-controlled tensile test. Mater Sci Engng [in press].
[14] Cao R, Lei MX, Chen JH, Zhang J. Effects of loading rate on damage and fracture behavior of TiAl alloy. Mater Sci Engng 2007;465(1–2):183–93.
[15] Chen JH, Cao R, Zhang J, Wang GZ. Fracture behaviour of precracked specimens of a TiAl alloy. Mater Sci Technol 2005;21(5):507–16.
[16] Chen JH, Pippan R, Hebesberger T. The fracture behaviour of intermetallic TiAl alloys with and without warm pre-stressing. Int J Fracture 2002;113(4):327–43.
[17] Chan KS, Kim YW. Influence of microstructure on crack tip micromechanics and fracture behaviors of a two-phase TiAl alloy. Metall Trans A 1992;23(6):1663–77.
[18] Liu CT, Schneibel JH, Maziasz PJ, Wright JL, Easton DS. Tensile properties and fracture toughness of TiAl alloys with controlled microstructure. Intermetallics 1996;4:429–40.